Supporting Information

$[(C_5H_6N_2)_2H](Sb_4F_{13})$: A polyfluoroantimonite with strong second harmonic generation effect

Jia-Hang Wu,[a,b] Chun-Li Hu,[a,c] Ya-Feng Li,[b] Jiang-Gao Mao[a,c] and Fang Kong [a,c]*

[a] State Key Laboratory of Structural Chemistry, Fujian Institute of Research on the Structure of Matter, Chinese Academy of Sciences, Fuzhou 350002, P. R. China

[b] College of Chemistry, Fuzhou University, Fuzhou 350108, P. R. China

[c] University of Chinese Academy of Sciences, Beijing 100049, P. R. China

Table of Contents

Experimental Procedures.

Reagents.

The chemical reagents 3-pyridinecarboxamide (3PC, $C_6H_6N_2O$) (98%, AR), 3-Aminopyridine (3AP, $C_5H_6N_2$) (99.8%, AR), SbF_3 (98%, AR), Ethylene Glycol (99+%, AR) and HF (40+%, AR) were obtained from Aladdin Chemistry. ***Caution:*** *hydrofluoric acid is toxic and corrosive! It must be handled with extreme caution and with the appropriate protective equipment and training.*

Syntheses.

Antimony trifluoride SbF_3 (1.780 g, 10 mmol) and 3-pyridinecarboxamide (0.476 g, 5 mmol) were dissolved in 10 mL ethylene glycol and 1 mL HF at room temperature. The mixture was allowed to evaporate slowly at room temperature and rod-shaped colorless crystals of $(3PC)_2(Sb_4F_{14})$ were isolated in high yields of > 85% (based on $C_6H_6N_2O$) after 2 weeks (Figure S1a). When using 3-aminopyridine to replace 3-pyridinecarboxamide, follow the same procedure, molar ratio, and solvent to obtain the light yellow crystals of $(3AP)_2(Sb_4F_{13})$ after 2 months (Figure S1b), with a yield greater than 70% (based on $C_5H_6N_2$). Powder XRD analyses confirmed the purity of the product (Figure S5). The presence of Sb, F, C and N elements were confirmed by energy-dispersive X-ray spectroscopy (EDS) analysis in the two compounds (Figure S4).

Single-Crystal Structure Determination.

Single crystal X-ray diffraction data of $(3PC)_2(Sb_4F_{14})$ and $(3AP)_2(Sb_4F_{13})$ were obtained on a Agilent Technologies SuperNova dual-wavelength CCD diffractometer with a graphite-

monochromated Mo Kα radiation (λ = 0.71073 Å) at room temperature. Cell refinement and data reduction were performed using *CrysAlisPro*. The structures were determined by the direct method and refined by full-matrix least-squares fitting on F^2 using *SHELXLTL*-17 crystallographic software package.[1, 2] The structural data were also checked by PLATON.[3]

Powder X-ray Diffraction. Powder X-ray Diffraction (PXRD) analysis was performed at room temperature. A Rigaku Miniflex600 diffractometer equipped with graphite mono-chromator Cu Kα radiation (λ = 1.54186 Å) was used to complete the measurement. The 2θ range is set to 5−60°, and the scan step size is 0.02°.

Energy-Dispersive X-ray Spectroscopy. Microprobe elemental analysis was carried out with the aid of a field-emission scanning electron microscope (JSM6700F) outfitted with an energy-dispersive X-ray spectroscope (Oxford INCA).

Spectroscopic Measurements. IR spectrum was measured by Magna 750 FT-IR spectrometer under the air background, and the selected range is 4000−400 cm^{-1}. UV-vis-NIR diffuse reflectance spectrum was recorded by a PerkinElmer Lambda 950 UV-vis-NIR spectrophotometer with $BaSO_4$ powder board as a reference for 100% reflectance, and the recording range was 200−1600 nm.[4] Absorption data was calculated from the diffuse reflection data by the Kubelka-Munk function: $\alpha/S = (1-R)^2/2R$, where α and S represent the absorption coefficient and the scattering coefficient, respectively. The band gap value can be given by extrapolating the absorption edge to the baseline in the α/S vs. energy graph. Photoluminescence (PL) excitation and emission spectra were measured on the FLS980 spectrometer (Edinburgh) equipped with both continuous (450 W) and pulsed xenon lamps. A

standard tungsten lamp was used to correct the optical response of the instrument.

Thermal Analysis. Thermogravimetric analyses (TGA) were performed in a nitrogen atmosphere using the NETZCH STA 449F3 thermal analyzer with an empty Al_2O_3 crucible (the empty crucible was used as a reference) as a reference. The powder samples were heated in the crucible from 20°C to 800°C at a rate of 10°C min^{-1}.

Birefringence Test. The birefringences of $(3PC)_2(Sb_4F_{14})$ and $(3AP)_2(Sb_4F_{13})$ were characterized by using the polarizing microscope equipped (ZEISS Axio Scope. A1) with Berek compensator. The wavelength of the light source was 546 nm. Owing to the clear boundary lines of the first-, second- and third-order interference color, the relative error was small enough. Before the scanning, the small and transparent $(3PC)_2(Sb_4F_{14})$ and $(3AP)_2(Sb_4F_{13})$ lamellar crystals were chosen to measure, in order to improve the accuracy of the birefringence.

The formula for calculating the birefringence is listed below,

$$R = | N_e - N_o | \times T = \Delta n \times T \qquad \text{Eq. (1)}$$

Here, R represents the optical path difference, Δn means the birefringence, and T denotes the thickness of the crystal.[5]

SHG Measurement. Powder SHG measurements were conducted using a modified method of Kurtz and Perry. Irradiation laser (λ = 1.064 μm) is generated by a Nd: YAG solid-state laser equipped with a Q switch. The $(3AP)_2(Sb_4F_{13})$ pure crystal samples ground into powder were sieved according to six different particle size ranges (45−53, 53−75, 75−105, 105−150,

150−210 and 210−300 μm). KH_2PO_4 (KDP) samples in the same size range were also be prepared, which were used as reference. SHG signals oscilloscope traces of $(3AP)_2(Sb_4F_{13})$ and KDP samples in the particle size range (150−210 μm) were recorded.

LIDT Measurement. The laser-induced damage threshold (LIDT) measurements of $(3AP)_2(Sb_4F_{13})$ crystal samples were performed by a Q-switched pulsed laser. The particle size range of the tested sample is 150−210 μm, the laser wavelength is 1064 nm; the pulse duration is 10 ns; the pulse frequency is 1 Hz and the laser spot area focused on the sample is 2.01 mm^2. The energy of the laser emission was gradually increased during the measurement, and the LIDT of the sample was determined when it turned black in color under the laser.

Computational Method. Single-crystal structural data of compounds $(3PC)_2(Sb_4F_{14})$ and $(3AP)_2(Sb_4F_{13})$ were used for the theoretical calculations. The electronic structures were performed using a plane-wave basis set and pseudo-potentials within density functional theory (DFT) implemented in the total-energy code CASTEP.[6, 7] For the exchange and correlation functional, we chose Perdew–Burke–Ernzerhof (PBE) in the generalized gradient approximation (GGA).[8] The interactions between the ionic cores and the electrons were described by the ultrasoft pseudopotential.[9] The following valence-electron configurations were considered in the computation: Sb-$5s^25p^3$, F-$2s^22p^5$, C-$2s^22p^2$, N-$2s^22p^3$, O-$2s^22p^4$ and H-$1s^2$. The numbers of plane waves included in the basis sets were determined by cutoff energy of 850 eV for $(3PC)_2(Sb_4F_{14})$ and $(3AP)_2(Sb_4F_{13})$. The numerical integration of the Brillouin zone were performed using Monkhorst-Pack k-point sampling of 2 × 2 × 1 and 3 × 3 × 2. The other parameters and convergent criteria were the default values of CASTEP code. To further

compare the optical properties of the conventional functional groups with the $3PC^+$ and $3AP^+$ cation, their electronic structures in molecular level were calculated through DFT method implemented by Gaussian09 package with the hybrid B3LYP functional at 6-31G(d,p) level.

The calculations of second-order NLO properties were based on length-gauge formalism within the independent particle approximation.[10] We adopted Chen's static formula, which was derived by Rashkeev et al.[11] and later improved by Chen's group. The second-order NLO susceptibility can be expressed as:

$$\chi^{\alpha\beta\gamma} = \chi^{\alpha\beta\gamma}(\mathrm{VE}) + \chi^{\alpha\beta\gamma}(\mathrm{VH}) + \chi^{\alpha\beta\gamma}(\text{two bands}) \qquad \text{Eq. (2)}$$

where $\chi^{\alpha\beta\gamma}$ (VE) and $\chi^{\alpha\beta\gamma}$ (VH) contribute to $\chi^{\alpha\beta\gamma}$ from virtual-electron processes and virtual-hole processes, respectively, and $\chi^{\alpha\beta\gamma}$ (two bands) contributes to $\chi^{\alpha\beta\gamma}$ from the two-band processes. The formulae for calculating $\chi^{\alpha\beta\gamma}$ (VE), and $\chi^{\alpha\beta\gamma}$ (VH), are given in ref [12].

The calculations of linear optical properties in terms of the complex dielectric function $\varepsilon(\omega) = \varepsilon 1(\omega) + i\varepsilon 2(\omega)$ were made. The imaginary part of the dielectric function ε2 was given in the following equation:

$$\varepsilon^{ij}{}_2(\omega) = \frac{8\pi^2 h^2 e^2}{(m^2 V)} \sum k \sum \mathrm{cv}(f_c - f_v) \frac{p^i_{cv}(k) p^j_{cv(k)}}{E^2_{vc}} \delta\,[E_c(k) - E_v(k) - h\omega] \qquad \text{Eq. (3)}$$

The f_c and f_v represent the Fermi distribution functions of the conduction and valence band. The term $p^i_{cv}(k)$ denotes the momentum matrix element transition from the energy level c of the conduction band to the level v of the valence band at the *k*th point in the Brillouin zone (BZ), and *V* is the volume of the unit cell.

The real part $\varepsilon_1(\omega)$ of the dielectric function $\varepsilon(\omega)$ follows from the Kramer–Kronig relationship. All the other optical constants may be derived from $\varepsilon_1(\omega)$ and $\varepsilon_2(\omega)$. For example, the refractive

index n(ω) can be calculated using the following expression:

$$n(\omega)= \left(\frac{1}{\sqrt{2}}\right) \left[\sqrt{\varepsilon_1^2(\omega) + \varepsilon_2^2(\omega) + \varepsilon_1(\omega)}\right]^{1/2} \qquad \text{Eq. (4)}$$

Table S1. Summary of crystal data and structural refinements for $(3PC)_2(Sb_4F_{14})$ and $(3AP)_2(Sb_4F_{13})$.

molecular formula	$(3PC)_2(Sb_4F_{14})$	$(3AP)_2(Sb_4F_{13})$
Formula Weight	499.64	923.24
crystal system	Triclinic	Triclinic
space group	*P*-1	*P*1
Temperature(K)	295.68(10)	250(10)
F(000)	460.0	422.0
a/Å	7.3227(10)	7.2222(3)
b/Å	7.4727(12)	8.1293(4)
c/Å	11.1037(16)	10.3779(4)
α(deg)	75.512(13)	101.002(4)
β(deg)	83.357(11)	105.247(4)
γ(deg)	85.846(13)	106.829(4)
V/Å^3	583.73(15)	538.65(4)
Z	2	1
Dc(g.cm^{-3})	2.843	2.846
GOF on F^2	0.995	1.045
R_1,wR_2[$I > 2\sigma(I)$]$^{\alpha}$	0.0303, 0.0536	0.0244, 0.0485
R_1, wR_2 (all data)$^{\alpha}$	0.0434, 0.0620	0.0261, 0.0504

$^{\alpha}$ $R_1 = \sum||F_o| - |F_c||/\sum|F_o|$, $wR_2 = \{\sum w[(F_o)^2 - (F_c)^2]^2/\sum w[(F_o)^2]^2\}^{1/2}$

Table S2. Atomic coordinates ($\times 10^4$) and equivalent isotropic displacement parameters ($Å^2 \times 10^3$) for $(3PC)_2(Sb_4F_{14})$ and $(3AP)_2(Sb_4F_{13})$. U_{eq} is defined as 1/3 of the trace of the orthogonalised U_{ij} tensor.

Compounds	Atom	x	y	z	U(eq)
$(3PC)_2(Sb_4F_{14})$	Sb(1)	7580.4(4)	3832.3(4)	4530.5(2)	27.87(13)
	Sb(2)	3015.9(5)	1943.9(5)	3590.2(3)	27.85(13)
	F(1)	8370(5)	5189(4)	5790(2)	48.9(8)
	F(2)	8906(4)	1733(4)	5487(2)	37.5(7)
	F(3)	5472(4)	3397(5)	5760(3)	52.8(9)
	F(4)	6363(5)	1792(5)	3958(3)	54.4(9)
	F(5)	3971(5)	3910(4)	2280(3)	59.1(10)
	F(6)	4063(4)	340(4)	2539(2)	45.4(8)
	F(7)	787(5)	2169(5)	2764(3)	60.8(10)
	C(1)	-1703(7)	8073(7)	1693(4)	31.2(12)
	C(2)	210(6)	7756(6)	1116(4)	23.3(10)
	C(3)	424(7)	7288(7)	-32(4)	34.2(12)
	C(4)	2160(8)	7028(8)	-600(4)	41.8(14)
	C(5)	3654(7)	7258(7)	-41(4)	35.8(13)
	C(6)	1753(6)	7953(7)	1646(4)	28.1(11)
	N(1)	3416(6)	7708(6)	1062(3)	33.0(10)
	N(2)	-1927(6)	8800(7)	2677(3)	45.6(13)
	O(1)	-2985(5)	7678(7)	1221(4)	66.3(14)
$(3AP)_2(Sb_4F_{13})$	Sb(1)	3972.2(9)	5369.4(8)	6313.3(6)	28.41(16)
	Sb(2)	7727.7(9)	2732.8(7)	5306.9(6)	26.82(16)
	Sb(3)	5938.9(9)	-2602.8(8)	3650.0(6)	27.18(16)
	Sb(4)	2312.6(9)	-1239.0(8)	4700.3(6)	27.11(16)
	F(1)	3916(10)	7978(8)	6856(6)	35.5(15)
	F(2)	5208(14)	6021(11)	8321(8)	57(2)
	F(3)	6558(8)	6636(8)	6155(6)	39.0(14)
	F(4)	5291(12)	3415(9)	6416(8)	58.6(19)
	F(5)	9978(11)	4190(9)	7058(6)	50.2(18)
	F(6)	7117(9)	972(7)	6275(5)	34.9(13)
	F(7)	9661(10)	1653(9)	4866(7)	50.6(17)
	F(8)	5164(10)	158(9)	3594(6)	47.3(16)
	F(9)	4597(14)	-3024(11)	1677(7)	59(2)
	F(10)	5269(10)	-5206(8)	3212(6)	46.2(17)
	F(11)	3384(10)	-3042(9)	4045(6)	44.9(15)
	F(12)	53(9)	-3198(9)	4760(7)	46.3(16)
	F(13)	569(11)	-1616(10)	2792(7)	46.0(18)

	C(1)	8030(20)	3515(16)	10467(12)	36(3)
	C(2)	8989(19)	3080(18)	11642(12)	40(3)
	C(3)	8770(20)	1350(18)	11600(12)	44(3)
	C(4)	7550(20)	-18(19)	10392(15)	53(4)
	C(5)	6790(18)	2040(19)	9257(12)	44(3)
	C(6)	2140(20)	1716(19)	-452(13)	45(3)
	C(7)	980(20)	150(20)	-1639(13)	55(4)
	C(8)	830(20)	-1480(20)	-1536(16)	55(4)
	C(9)	1810(20)	-1820(20)	-345(16)	59(4)
	C(10)	3060(20)	1330(20)	757(13)	49(4)
	N(1)	6626(16)	402(14)	9264(11)	40(3)
	N(2)	8150(20)	5172(15)	10460(12)	64(4)
	N(3)	2901(17)	-325(17)	780(11)	47(3)
	N(4)	2350(20)	3329(16)	-457(14)	68(3)

Table S3. The bond lengths (Å) and calculated bond valences for $(3PC)_2(Sb_4F_{14})$ and $(3AP)_2(Sb_4F_{13})$.

Compounds	Bond	Bond-length	Bond-valence	BVS
$(3PC)_2(Sb_4F_{14})$	Sb(1)-F(1)	2.074(3)	0.625	3.093
	Sb(1)-F(2)	1.928(3)	0.927	
	Sb(1)-F(3)	1.927(3)	0.930	
	Sb(1)-F(4)	2.082(3)	0.611	
	Sb(2)-F(4)	2.521(3)	0.187	3.181
	Sb(2)-F(5)	1.900(3)	1.000	
	Sb(2)-F(6)	1.935(3)	0.910	
	Sb(2)-F(7)	1.940(3)	0.897	
	Sb(2)-F(1)#1	2.520(3)	0.187	
$(3AP)_2(Sb_4F_{13})$	Sb(1)-F(1)	2.103(6)	0.578	3.045
	Sb(1)-F(2)	1.936(7)	0.907	
	Sb(1)-F(3)	1.920(6)	0.947	
	Sb(1)-F(4)	2.081(6)	0.613	
	Sb(2)-F(4)	2.473(7)	0.213	3.104
	Sb(2)-F(5)	1.964(6)	0.841	
	Sb(2)-F(6)	1.915(5)	0.960	
	Sb(2)-F(7)	1.955(6)	0.862	
	Sb(2)-F(8)	2.361(7)	0.288	
	Sb(3)-F(8)	2.473(7)	0.212	2.857
	Sb(3)-F(9)	1.936(6)	0.907	
	Sb(3)-F(10)	1.961(6)	0.848	
	Sb(3)-F(11)	1.943(6)	0.890	
	Sb(4)-F(11)	1.940(6)	0.898	2.818
	Sb(4)-F(12)	1.947(6)	0.881	
	Sb(4)-F(13)	1.959(6)	0.853	
	Sb(4)-F(1)#1	2.522(6)	0.186	

Symmetry transformations used to generate equivalent atoms:

For $(3PC)_2(Sb_4F_{14})$:
#1 1-x, 1-y, 1-z.

For $(3AP)_2(Sb_4F_{13})$:
#1 +x, -1+y, +z.

Table S4. Selected Hydrogen bond lengths (Å) and angles (°) for $(3PC)_2(Sb_4F_{14})$ and $(3AP)_2(Sb_4F_{13})$.

Compounds	D − H…A	d(D − H)	d(H…A)	d(D…A)	∠(D − H…A)
$(3PC)_2(Sb_4F_{14})$	N2 − H2a…F6	0.86	2.35	3.108(6)	143.7
	N2 − H2b…F2	0.86	2.35	3.117(5)	149
	C6 − H6…F2	0.93	2.32	3.229(5)	165.8
$(3AP)_2(Sb_4F_{13})$	N1 − H1…F1	0.87	1.84	2.697(12)	167
	N2 − H2a…F13	0.87	2.04	2.907(14)	171
	C1 − H10…F10	0.94	2.16	3.080(15)	167

Table S5. Calculation of dipole moment for SbF_4, SbF_5, Sb_4F_{13} and net dipole moment for a unit cell in $(3AP)_2(Sb_4F_{13})$.

Compounds	**groups**	**Dipole moment (D)**			
		total magnitude	**x-component**	**y-component**	**z-component**
$(3AP)_2(Sb_4F_{13})$	$Sb(1)F_4$	10.189	6.876	3.529	6.639
	$Sb(2)F_5$	8.719	1.558	-7.063	4.870
	$Sb(3)F_4$	19.160	-14.582	-5.348	-11.230
	$Sb(4)F_4$	8.988	-0.179	-8.254	-3.553
	Sb_4F_{14}	18.558	-6.327	-17.136	-3.274
	Net dipole moment (a unit cell)	18.558	-6.327	-17.136	-3.274

Table S6. The assignment of the IR absorption peaks for $(3PC)_2(Sb_4F_{14})$ and $(3AP)_2(Sb_4F_{13})$.

Assignment (cm^{-1})	**$(3PC)_2(Sb_4F_{14})$**	**$(3AP)_2(Sb_4F_{13})$**
ν(N – H)	3455, 3342	3451, 3363, 3250
ν(C – H)	3070-2850, 1050-650	3070-2880, 1010-650
ν(C – C)	1690-1380	1690-1400
ν(C – N)	1350-1110	1350-1140
ν(Sb – F)	600-450	600-450

Table S7. All the fluoroantimonite compounds with SHG effect and the coordination mode of Sb^{3+}.

Compounds	**Coordination mode of Sb^{3+}**	**SHG effect**	**Ref.**
$K_2SO_4{\cdot}SbF_3$	SbO_2F_3	0.1 × KDP	[13]
$Rb_2SO_4{\cdot}SbF_3$	SbO_2F_3	0.3 × KDP	[13]
$CsSbClF_3$	$SbCl_2F_3$	0.3 × KDP	[14]
$Rb_2SO_4{\cdot}(SbF_3)_2$	SbO_2F_3	0.5 × KDP	[15]
$NH_4SbF_2SO_4$	SbO_2F_2	0.7 × KDP	[16]
$RbSbF_2SO_4$	SbO_3F_3	0.96 × KDP	[17]
$Zn_3Sb_4O_6F_6$	SbO_3	40 × SiO2	[18]
$(NH_4)Sb_2(C_2O_4)F_5$	SbO_2F_2 + $SbOF_3$	1.1 × KDP	[19]
$RbSb_2(C_2O_4)F_5$	SbO_2F_2 + $SbOF_3$	1.3 × KDP	[20]
$(C_6H_6N)SbF_2SO_4$	SbO_2F_2	1.6 × KDP	[21]
$C(NH_2)_3SbF_4$	SbF_4	2.0 × KDP	[22]
$Rb_3SbF_3(NO_3)_2$	SbO_2F_3	2.2 × KDP	[23]
$Rb_2SbF_3(NO_3)_2$	SbO_3F_3 + SbO_2F_3	2.7 × KDP	[24]
$CsSbF_2SO_4$	SbO2F2	3.0 × KDP	[25]
$NaSb_3F_{10}$	SbF_3+SbF_4	3.2 × KDP	[26]
$(NH_4)_3SbF_3(NO_3)_3$	SbF_3	3.3 × KDP	[27]
$K_2Sb(P_2O_7)F$	SbO_4F	4.0 × KDP	[28]
$K_2SbF_2Cl_3$	SbF_2Cl_3	4.0 × KDP	[29]
$Rb_2Sb(P_2O_7)F$	SbO_4F	5.1 × KDP	[30]
$(3AP)_2(Sb_4F_{13})$	**SbF_4+SbF_5**	**8.1 × KDP**	**This work**
4-HPY($Sb_2O_2F_4$)	SbO_2F_2	12 × KDP	[31]

Table S8. SHG effect and energy bandgap of representative NLO organic-inorganic antimony halides.

Compounds	**SHG effect**	**Band gap (eV)**	**Thermal stability (℃)**	**Ref.**
(R/S-$C_5H_{14}N_2$)$SbCl_5$	1.93 × KDP	3.06	220	[32]
($C_9H_{14}N$)$SbCl_4$	2.1 × KDP	3.47	147	[33]
$A_2Sb(C_2O_4)Cl_3$ (A=NH_4, K, Rb)	1.8, 1.6, 2.1 × KDP	3.55, 3.61, 3.74	80, 205, 225	[34]
($C_7H_{15}NCl$)$SbCl_4$	0.53 × KDP	3.05	227	[35]
($C_4H_{10}NO$)$_2SbCl_5$	0.12 × KDP	3.25	202	[36]
($C_6H_{14}N$)$_2SbCl_5$	0.3 × KDP	–	204	[37]
($C_9H_{26}N_3$)$SbCl_6$	1.3 × KDP	3.24	180	[38]
(L-Hhis)$_2Sb_2Cl_8$	0.1 × KDP	3.64	240	[38]
L-H_2his·$SbBr_5$·H2O	2.6 × KDP	2.73	75	[38]
(L-H_2his)$_2$·Sb_3I_{13}·$4H_2O$	0.05 × KDP	2.20	75	[39]
(3AP)$_2$(Sb_4F_{13})	**8.1 × KDP**	**3.05**	**153**	**This work**

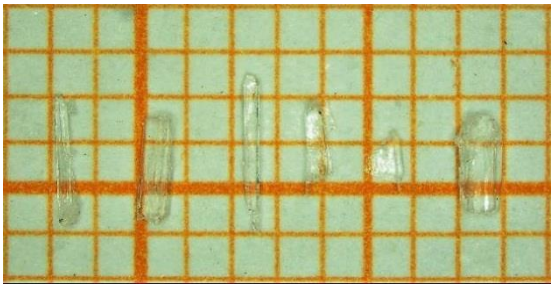

(a)

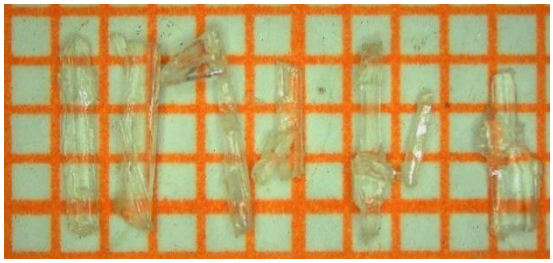

(b)

Figure S1. As-grown small crystals of $(3PC)_2(Sb_4F_{14})$ and $(3AP)_2(Sb_4F_{13})$.

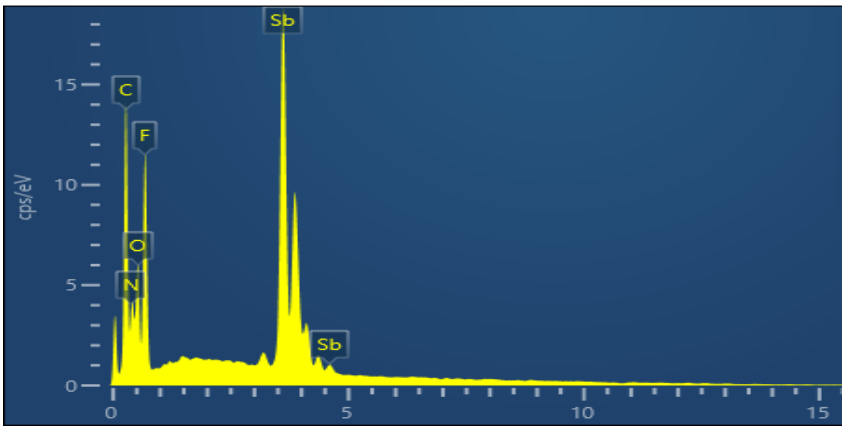

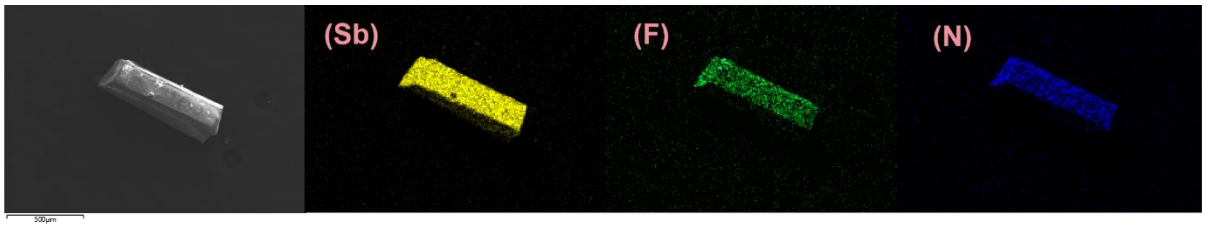

(a)

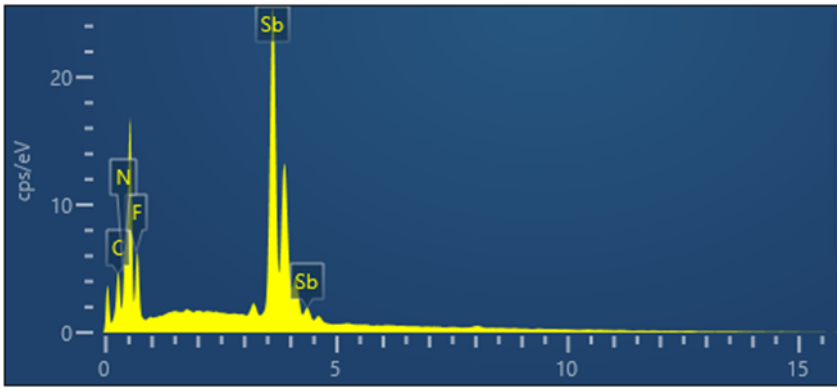

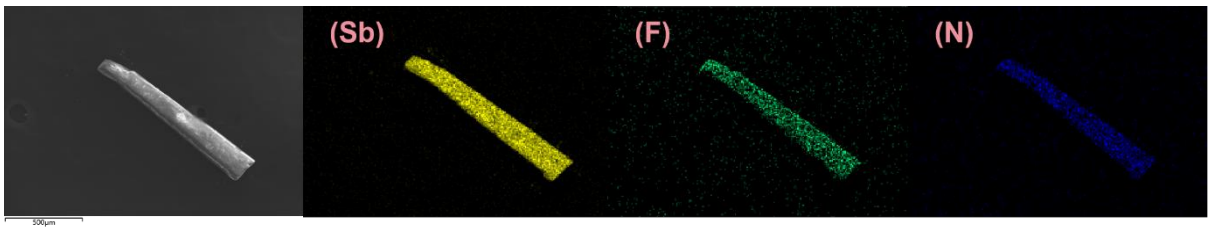

(b)

Figure S2. Energy dispersive spectrum analysis and element distribution maps for $(3PC)_2(Sb_4F_{14})$ (a) and $(3AP)_2(Sb_4F_{13})$ (b).

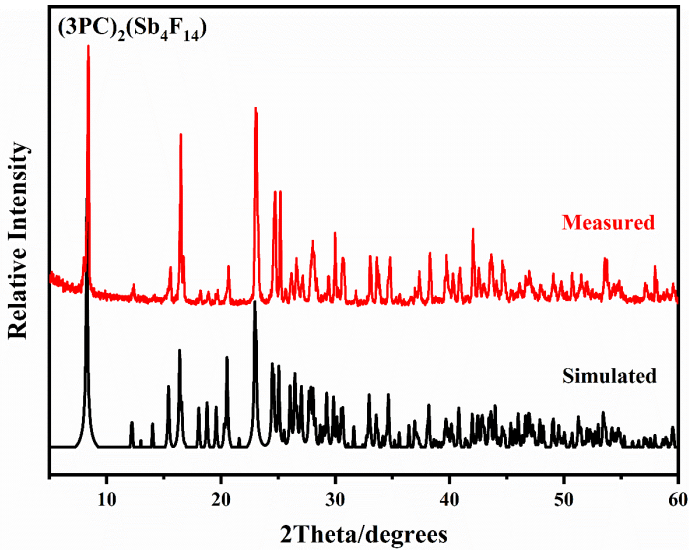

(a)

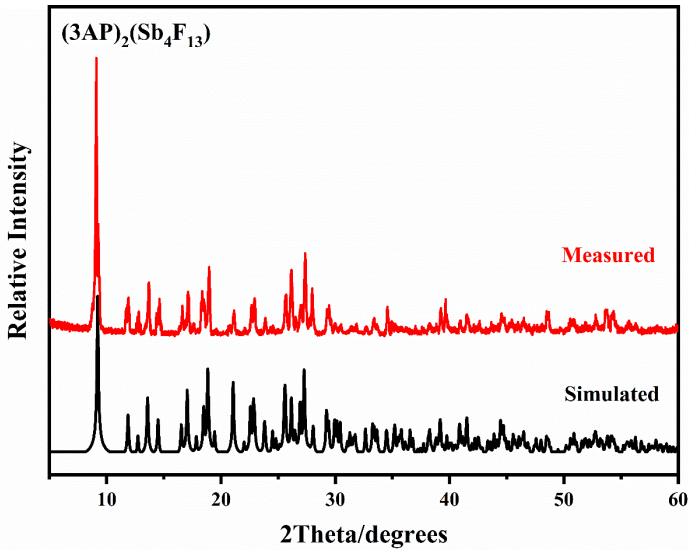

(b)

Figure S3. Simulated and measured powder X-ray diffraction patterns of $(3PC)_2(Sb_4F_{14})$ (a) and $(3AP)_2(Sb_4F_{13})$ (b).

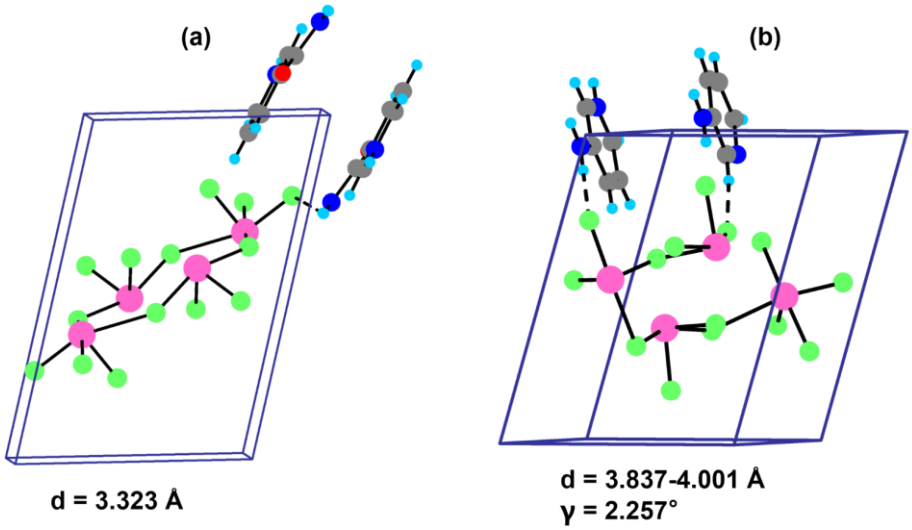

Figure S4. Detailed structure views of $(3PC)_2(Sb_4F_{14})$ (a) and $(3AP)_2(Sb_4F_{13})$ (b): π– π stacking, the dihedral angles (γ) and inter-ring distances between adjacent organic amines.

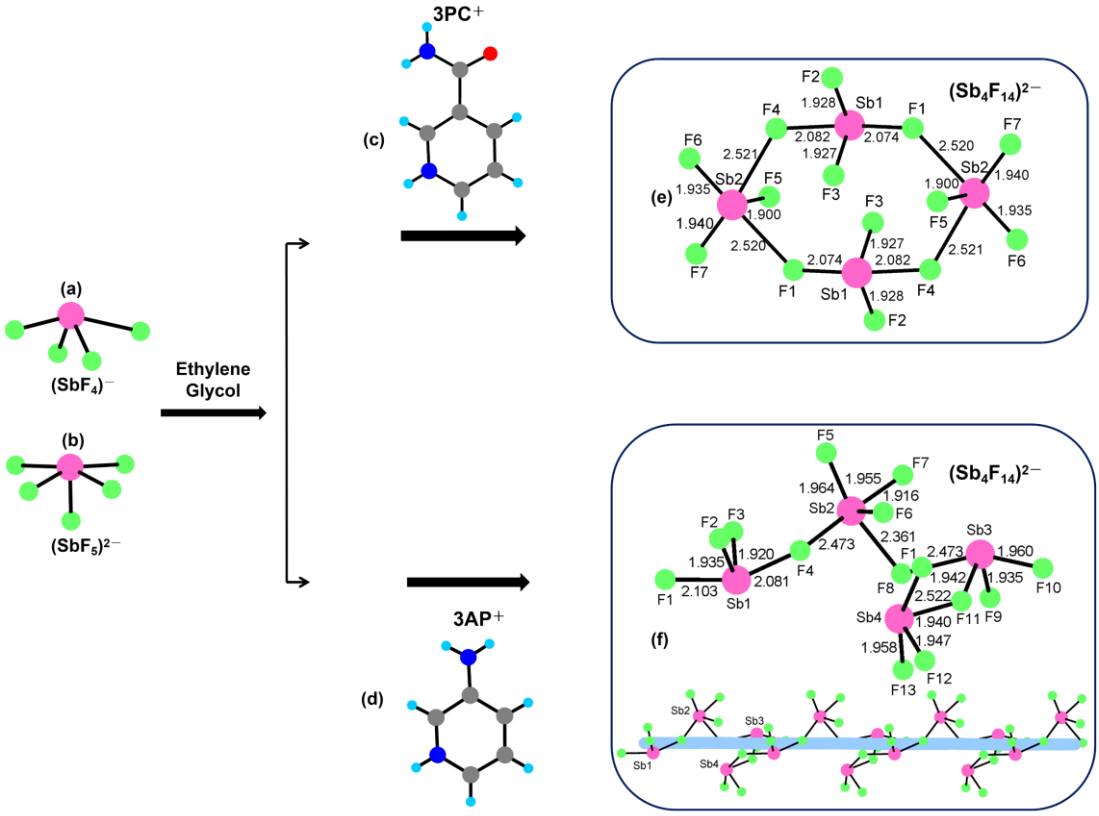

Figure S5. The schematic diagram of the formation of the different of polyfluoroantimonite groups.

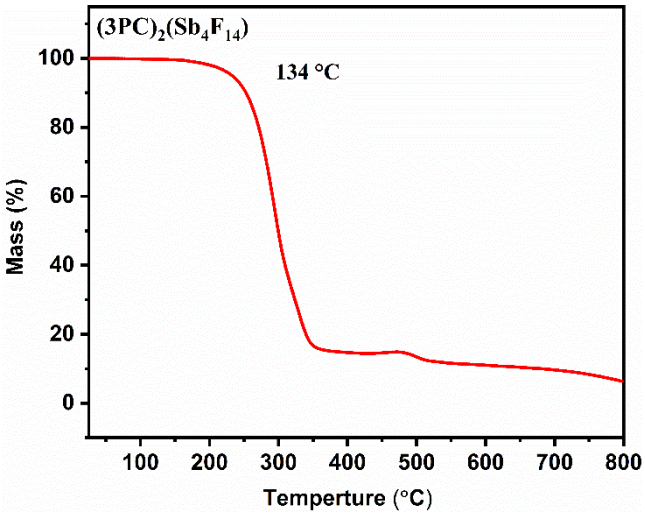

(a)

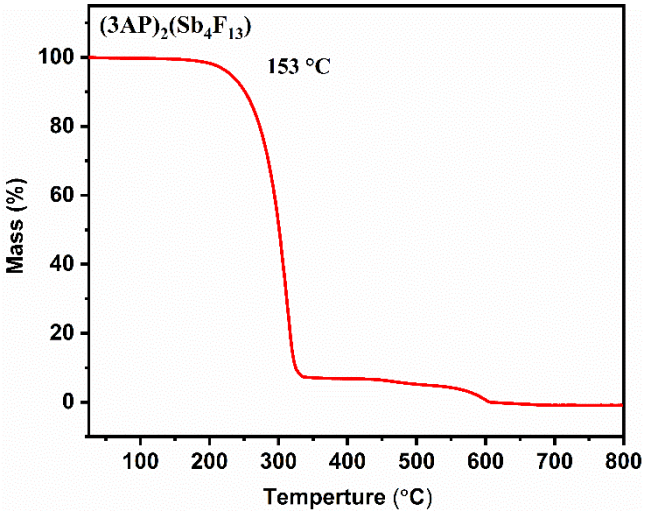

(b)

Figure S6. The TGA curves of $(3PC)_2(Sb_4F_{14})$ (a) and $(3AP)_2(Sb_4F_{13})$ (b).

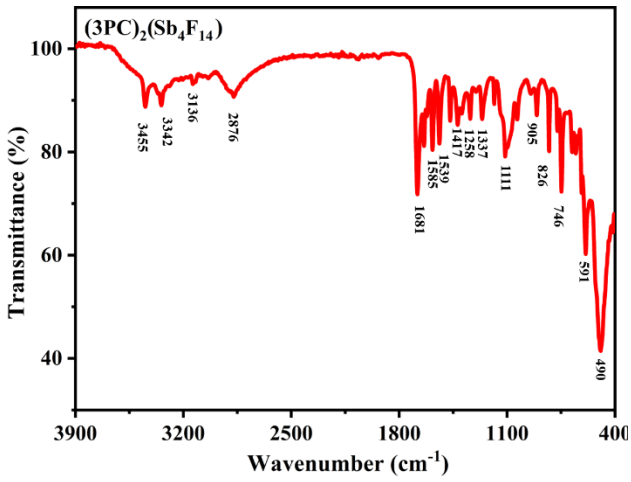

(a)

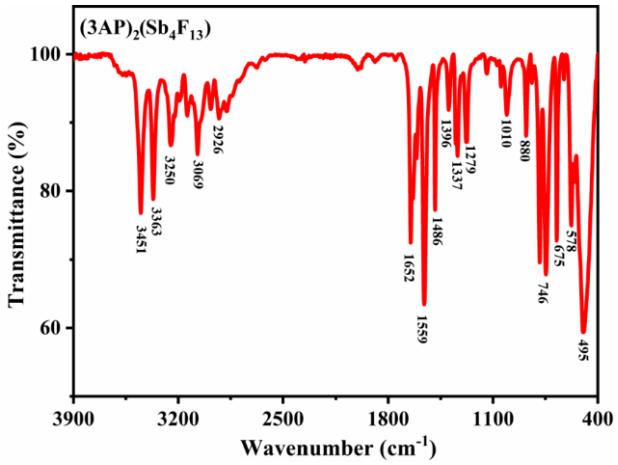

(b)

Figure S7. Infrared spectra of $(3PC)_2(Sb_4F_{14})$ (a) and $(3AP)_2(Sb_4F_{13})$ (b).

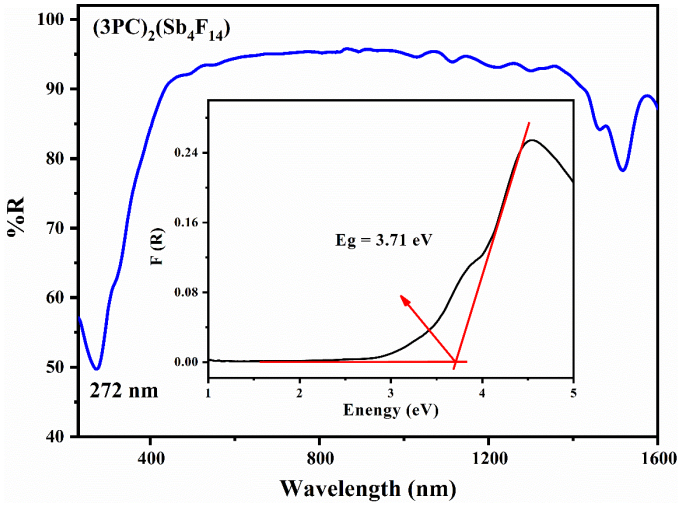

(a)

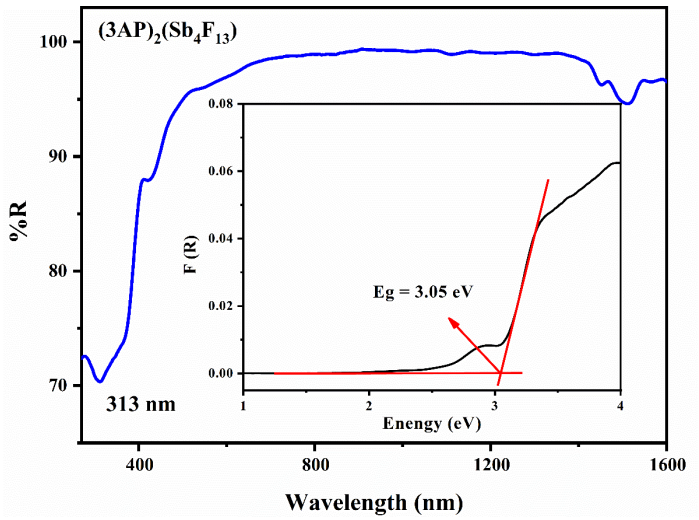

(b)

Figure S8. UV-vis-NIR diffuse reflectance spectra of $(3PC)_2(Sb_4F_{14})$ (a) and $(3AP)_2(Sb_4F_{13})$ (b).

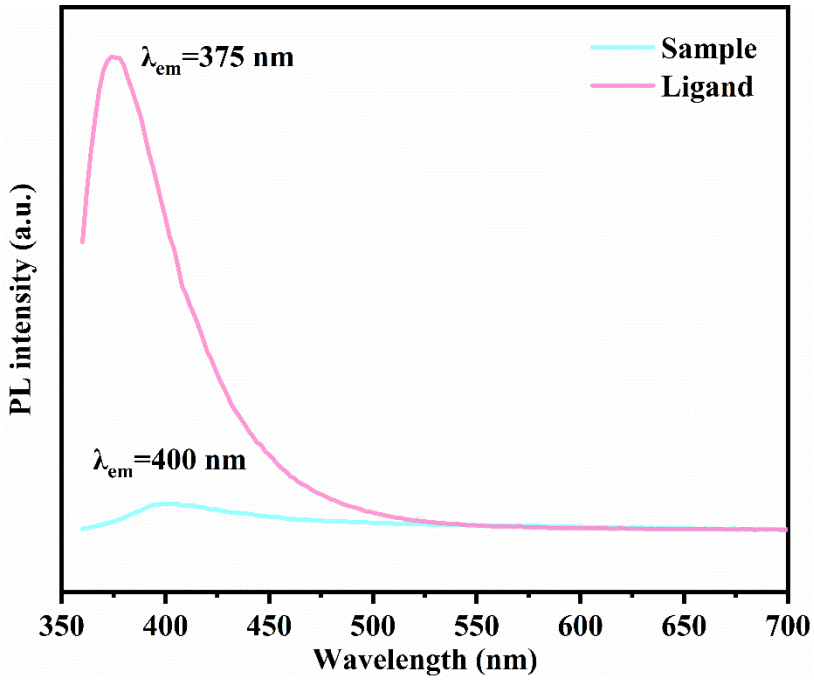

Figure S9. Fluorescence spectra for $(3AP)_2(Sb_4F_{13})$ and 3AP under excitation at 330 nm.

(a)

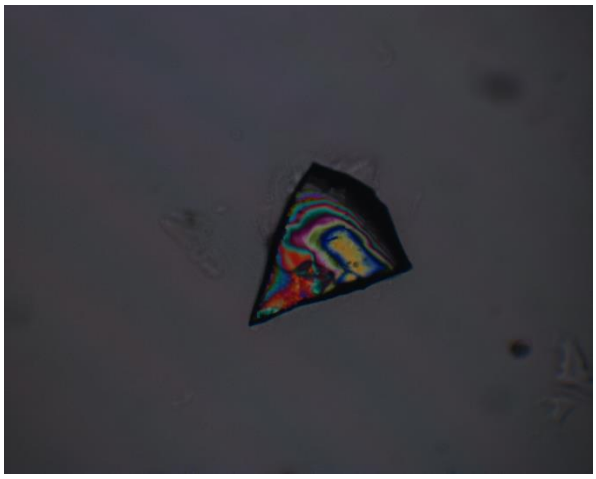

(b)

(c)

Figure S10. original crystal of $(3PC)_2(Sb_4F_{14})$ under the ortho-polarized light (a), crystal achieving complete extinction (b) and the crystal thickness (c) of $(3PC)_2(Sb_4F_{14})$ used for birefringence measurement.

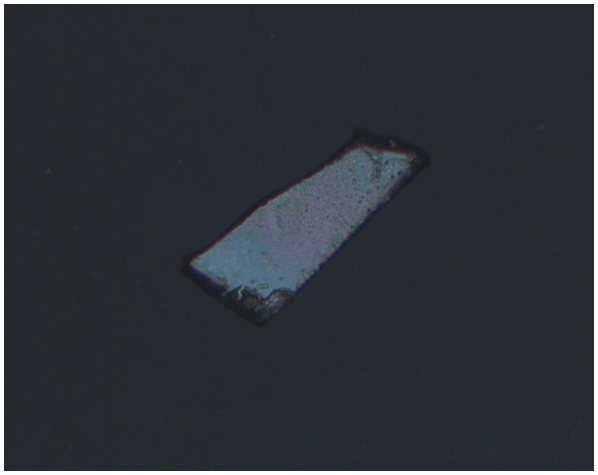

(a)

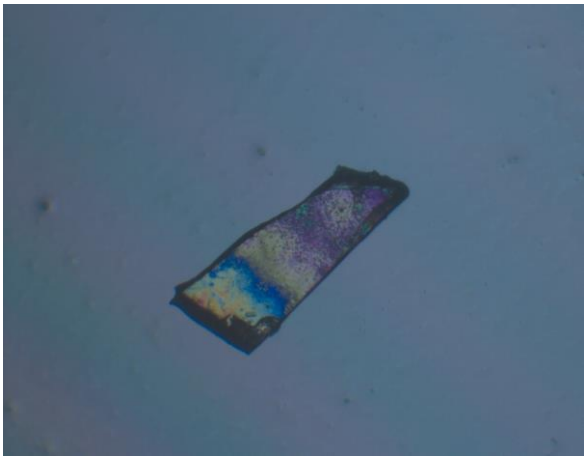

(b)

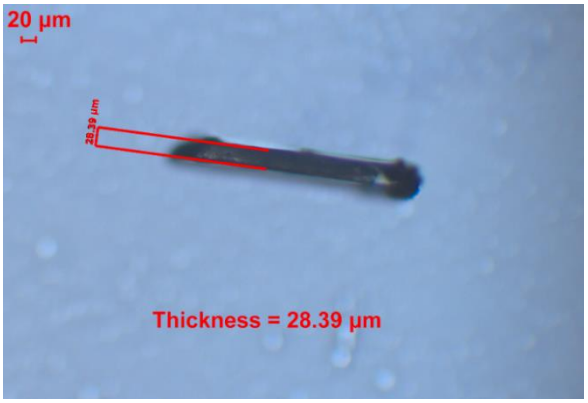

(c)

Figure S11. original crystal of $(3AP)_2(Sb_4F_{13})$ under the ortho-polarized light (a), crystal achieving complete extinction (b) and the crystal thickness (c) of $(3AP)_2(Sb_4F_{13})$ used for birefringence measurement.

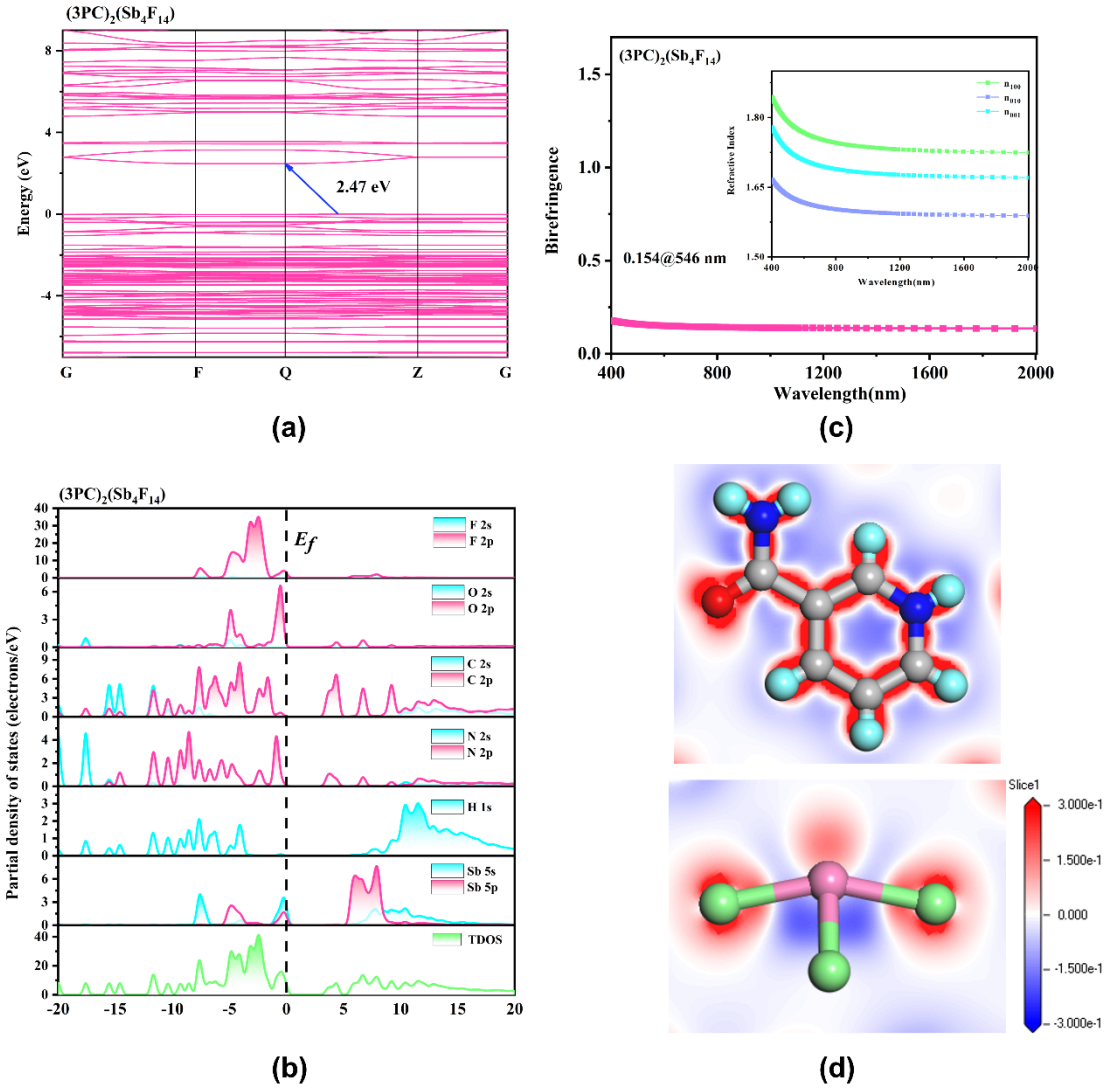

Figure S12. The band structure (a), total and partial density of states (b), birefringence (c) and electron density difference maps (d) for $(3PC)_2(Sb_4F_{14})$.

References

[1] G. M. Sheldrick, *Acta Crystallogr. Sect. C: Cryst. Struct. Commun.* **2015**, *71*, 3-8.

[2] R. H. Blessing, *Acta Crystallogr.* **1995**, *A51*, 7-13.

[3] A. L. Spek, J. *Appl. crystallogr.* **2003**, *36*, 7-13.

[4] J. Tauc, *Mater. Res. Bull.* **1970**, *5*, 721-729.

[5] L. L. Cao, G. Peng, W. B. Liao, T. Yan, X. F. Long, N. Ye, *CrystEngComm.* **2020**, *22 (11)*, 1956-1961.

[6] M. D. Segall, P. J. D. Lindan, M. J. Probert, C. J. Pickard, P. J. Hasnip, S. J. Clark, M. C. Payne, *J. Phys.: Condens. Matter* **2002**, *14*, 2717-2744.

[7] V. Milman, B. Winkler, J. A. White, C. J. Pickard, M. C. Payne, E. V. Akhmatskaya, R. H. Nobes, *Int. J. Quantum Chem.* **2000**, *77 (5)*, 895-910.

[8] J. P. Perdew, K. Burke, M. Ernzerhof, *Phys. Rev. Lett.* **1996**, *77*, 3865-3868.

[9] J. S. Lin, A. Qteish, M. C. Payne, V. Heine, *Matter Mater. phys.* **1993**, *47*, 4174-4180.

[10] C. Aversa, J. Sipe, *Phys. Rev. B: Condens. Matter Mater. Phys.* **1995**, *52*, 14636.

[11] S. N. Rashkeev, W. R. Lambrecht, B. Segall, *Phys. Rev. B: Condens. Matter Mater. Phys.* **1998**, 57, 3905.

[12] J. Lin, M. H. Lee, Z. P. Liu, C. Chen and C. J. Pickard, *Phys. Rev. B: Condens. Matter Mater. Phys.* **1999**, *60*, 13380.

[13] F. F. He, L. Wang, C. F. Hu, J. Zhou, Q. Li, L. Huang, D. J. Gao, J. Bi, X. Wang, G. Zou, *Dalton Trans.* **2018**, *47*, 17486-17492.

[14] P. F. Gong, Y. Yang, F. G. You, X. Y. Zhang, G. M. Song, S. Z. Zhang, Q. Huang, Z. S. Lin, *Cryst. Growth Des.* **2019**, *19*, 1874-1879.

[15] Q. Wang, L. Wang, X. Y. Zhao, L. Huang, D. J. Gao, J. Bi, G. H. Zou, *Inorg. Chem. Front.* **2019**, *6*, 3125-3132.

[16] F. F. He, Y. W. Ge, X. Y. Zhao, J. He, L. Huang, D. J. Gao, J. Bi, X. Wang, G. H. Zou, *Dalton Trans.* **2020**, *49*, 5276-5282.

[17] F. Yang, L. J. Huang, X. Y. Zhao, L. Huang, D. J. Gao, J. Bi, X. Wang, G. H. Zou, *J. Mater. Chem. C* **2019**, *7*, 8131-8138.

[18] S. I. Ali, W. Zhang, P. S. Halasyamani, M. Johnsson, *J. Solid State Chem.* **2017**, *256*, 158-161.

[19] D. Zhang, Q. Wang, T. Zheng, L. Huang, L. L. Cao, D. J. Gao, J. Bi, G. H. Zou, *J. Alloy. Compd.* **2022**, *896*, 162921.

[20] W. Y. Wang, X. Y. Wang, L. Xu, D. Zhang, J. L. Xue, S. Y. Wang, X. H. Dong, L. L. Cao, L. Huang, G. H. Zou, *Inorg. Chem.* **2023**, *62*, 13148-13155.

[21] P. Zhang, X. Mao, X. H. Dong, L. Huang, L. L. Cao, D. J. Gao, G. H. Zou, *Chinese Chem Lett.* **2023**. DOI: 10.1016/j.cclet.2023.109235

[22] M. Zhang, B. B. Zhang, D. Q. Yang, Y. Wang, *Inorg. Chem.* **2021**, *60*, 18483-18489.

[23] L. Wang, F. Yang, X. Y. Zhao, L. Huang, D. J. Gao, J. Bi, X. Wang, G. H. Zou, *Dalton Trans.* **2019**, *48*, 15144-15150.

[24] L. Wang, H. M. Wang, D. Zhang, D. J. Gao, J. Bi, L. Huang, G. H. Zou, *Inorg. Chem. Front.* **2021**, *8*, 3317-3324.

[25] X. H. Dong, L. Huang, C. F. Hu, H. M. Zeng, Z. E. Lin, X. Wang, K. M. Ok, G. H. Zou, *Angew. Chem. Int. Ed.* **2019**, *58*, 6528-6534.

[26] G. Zhang, J. G. Qin, T. Liu, Y. J. Li, Y. C. Wu, C. T. Chen, *Appl. Phys. Lett.* **2009**, *95*, 261104.

[27] Q. Wang, J. X. Ren, D. Wang, L. L. Cao, X. H. Dong, L. Huang, D. J. Gao, G. H. Zou, *Inorg. Chem. Front.* **2023**, *10*, 2107-2114.

[28] Y. L. Deng, L. Huang, X. H. Dong, L. Wang, K. M. Ok, H. M. Zeng, Z. E. Lin, G. H. Zou, *Angew. Chem. Int. Ed.* **2020**, *59*, 21151-21156.

[29] Y. Huang, X. G. Meng, P. F. Gong, Z. S. Lin, X. G. Chen, J. G. Qin, *J. Mater. Chem. C* **2015**, *3*, 9588-9593.

[30] X. H. Dong, H. B. Huang, L. Huang, Y. Q. Zhou, B. B. Zhang, H. M. Zeng, Z. E. Lin, G. H. Zou, *Angew. Chem. Int. Ed.* **2024**, e202318976.

[31] Q. Lu, X. X. Jiang, K. N. Duanmu, C. Wu, Z. S. Lin, Z. P. Huang, M. G. Humphrey, C. Zhang, *J. Am. Chem. Soc.* **2024**, *146*, 9975-9983.

[32] S. M. Qi, P. X. Cheng, X. Han, F. Ge, R. C. Shi, L. Xu, G. Li, J. L. Xu, *Cryst. Growth Des.* **2022**, *22*, 6545-6553.
[33] F. F. Wu, Q. Y. Wei, X. Q. Li, Y. Liu, W. Q. Huang, Q. Chen, B. X. Li, J. H. Luo, X. T. Liu, *Cryst. Growth Des.* , **2022**, *22*, 3875-3881.
[34] D. Zhang, Q. Wang, H. Luo, L. L. Cao, X. H. Dong, L. Huang, D. J. Gao, G. H. Zou, *Adv. Opt. Mater.* **2023**, *11*, 2202874.
[35] J. M. Gong, T. Shao, P. Z. Huang, C. Y. Su, M. Chen, D. W. Fu, H. F. Lu, *J. Phys. Chem. C.*, **2022**, *126*, 15274-15279.
[36] J. C. Zhuang, Y. H. Tan, X. W. Fan, Y. Z. Tang, N. Song, Y. H. Zhang, H. Zhang, S. P. Chen, *New J. Chem.* **2022**, *46*, 7103–7107.
[37] J. Zhang, S. G. Han, X. T. Liu, Z. Y. Wu, C. M. Ji, Z. H. Sun, J. H. Luo, *Chem. Commun.* **2018**, *54*, 5614–5617.
[38] X. M. Wen, J. Cheng, P. Q. Qian, Z. Z. Zhang, H. M. Zeng, L. Huang, G. H. Zou, Z. E. Lin, *Dalton Trans.* **2024**, *53*, 260-266.
[39] J. Cheng, P. Q. Qian, M. Yang, L. Huang, H. M. Zeng, G. H. Zou, Z. E. Lin, *Inorg. Chem.* **2023**, *62*, 16673-16676.